Available online at www.sciencedirect.com

ScienceDirect

Geochimica et Cosmochimica Acta 296 (2021) 152–169

Geochimica et Cosmochimica Acta

www.elsevier.com/locate/gca

Experimental determination of the effect of Cr on Mg isotope fractionation between spinel and forsterite

Haolan Tang [a,*], Ian Szumila [b], Dustin Trail [b], Edward D. Young [a]

[a] Department of Earth, Planetary, and Space Sciences, UCLA, Los Angeles, CA 90095, United States
[b] Department of Earth and Environmental Sciences, University of Rochester, Rochester, NY 14618, United States

Received 4 September 2020; accepted in revised form 30 December 2020; available online 12 January 2021

Abstract

We report the results of spinel-magnesite Mg isotope exchange experiments at 600, 700, and 800 °C and 1 GPa to establish the equilibrium Mg isotope partitioning between magnesite ($MgCO_3$) and spinel as a function of Cr substitution for Al in the spinel phase. We used the three-isotope method to obtain equilibrium fractionation factors between $MgAlCrO_4$ and magnesite and $MgCr_2O_4$ and magnesite. The experimentally-determined temperature-dependent Mg isotope fractionations are $\Delta^{26}Mg_{MgAlCrO_4\text{ - Mgs}} = 0.96 \pm 0.22 \times 10^6/T^2$ and $\Delta^{26}Mg_{MgCr_2O_4\text{ - Mgs}} = 0.55 \pm 0.08 \times 10^6/T^2$ (2 s.e.). When combined with the previous experimentally determined fractionation between forsterite and magnesite (Macris et al., 2013), the corresponding Mg isotope fractionations between these two Cr-bearing spinel compositions and forsterite are $\Delta^{26}Mg_{MgAlCrO_4\text{ - Fo}} = 0.84 \pm 0.23 \times 10^6/T^2$ and $\Delta^{26}Mg_{MgCr_2O_4\text{ - Fo}} = 0.43 \pm 0.10 \times 10^6/T^2$. The experimentally determined isotopic fractionation relationship between magnesiochromite and magnesite agrees with theoretical predictions based on the crystal chemical environment of Mg in these minerals. By combining these new results with the existing experimental calibration of equilibrium Mg isotope exchange between pure spinel and forsterite, we arrive at the temperature-dependent Mg isotope fractionation between spinel and forsterite as a function of Cr concentration in the spinel:

$$\Delta^{26}Mg_{Mg(Al_{1-x}Cr_x)_2O_4\text{ - Fo}} = [(-0.67 \pm 0.26)x + 1.10 \pm 0.23]10^6/T^2$$

When applied to natural samples, the combination of measured Mg isotope fractionation between spinel and forsterite, the Cr concentrations of the spinels, and estimates of temperature from independent geothermometers can be used to identify differences in closure temperatures between Mg isotope exchange and cation exchange, or the presence of disequilibrium in these systems.

Keywords: Mg isotope fractionation; Spinel; Forsterite; High temperature experiment; Cr substitution

1. INTRODUCTION

High-temperature partitioning of the stable isotopes of major rock-forming elements, including magnesium, silicon, and iron, are useful new tools in geochemistry. Among the rock-forming elements, the isotopes of Mg hold particular promise as tracers of high-temperature processes in part because Mg is the third most abundant element in the bulk silicate Earth (Young and Galy, 2004). Small differences in $^{26}Mg/^{24}Mg$ among mantle spinel, pyroxene, and olivine led Young et al. (2009) to suggest that isotope partitioning could be used as a high-temperature geothermometer. At the same time, these authors suggested that

* Corresponding author.
E-mail address: haolantang@ucla.edu (H. Tang).

https://doi.org/10.1016/j.gca.2020.12.028
0016-7037/

the inter-mineral fractionations, while resolvable, are sufficiently small that differentiation was not an explanation for the differences between terrestrial mantle whole-rock Mg isotope ratios and chondritic ratios. This in turn suggests that the bulk silicate Earth (BSE) has an intrinsically higher $^{26}Mg/^{24}Mg$ than chondrites. Hin et al. (2017) used higher-precision whole-rock Mg isotope ratio measurements to show that Earth is indeed slightly higher in $^{26}Mg/^{24}Mg$ than chondrites. Taken together, these studies suggest that while there should be some Mg isotopic effects caused by differentiation, these effects may be small in comparison to differences in bulk $^{26}Mg/^{24}Mg$ between different solar system bodies (Hin et al., 2017; Young et al., 2019).

Applications of Mg isotope ratios in high-temperature rocks beyond these first-order observations requires a better understanding of the links between inter-mineral fractionation and changes in whole-rock Mg isotope ratios with differentiation. Small but resolvable Mg isotope fractionations among minerals in mantle xenoliths are now well documented (e.g., Wiechert and Halliday, 2007; Handler et al., 2009; Yang et al., 2009; Young et al., 2009; Huang et al., 2011; Li et al., 2011; Liu et al., 2011; von Strandmann et al., 2011; Wang et al., 2012; Xiao et al., 2013; Wang et al., 2014; Hu et al., 2016) and yet some studies have reported no resolvable Mg isotope fractionation between Earth's mantle (peridotite) and its derivative melts (MORB and OIB) (e.g., Teng et al., 2007; Bourdon et al., 2010; Teng et al., 2010; Dauphas et al., 2010; Huang et al., 2011). Other studies have suggested that terrestrial basalts have higher $^{26}Mg/^{24}Mg$ than ultramafic rocks (Hin et al., 2017; Young et al., 2019). In all cases, equilibrium fractionation factors among minerals and melts are crucial for understanding the potential effects of igneous differentiation on Mg isotope ratios.

Inter-mineral equilibrium isotopic fractionation factors can be predicted using crystal chemical principles (Young et al., 2015). For example, among the dominant mantle minerals, the greatest inter-mineral fractionation in the Mg isotopic system in mantle xenoliths occurs between spinel and forsterite because Mg is in octahedral coordination in forsterite but tetrahedral coordination in spinel (Young et al., 2009). These different bonding environments of Mg in forsterite and spinel result in a longer Mg-O bond length in forsterite (0.210 nm; Shannon, 1976) compared to that in spinel (0.195 nm, Shannon, 1976), and thus a stiffer Mg-O bond on average in spinel. Since heavy isotopes will accumulate on stiffer bonds at thermodynamic equilibrium, all else equal, spinel is expected to have higher $^{26}Mg/^{24}Mg$ than coexisting olivine. Likewise, Mg is in octahedral coordination with oxygen in orthopyroxene ($MgSiO_3$) and the mean Mg-O bond length is ~0.209 nm (Young et al., 2015, and references therein). Thus, one would predict that $^{26}Mg/^{24}Mg$ ratios in orthopyroxene should be intermediate between those of spinel and olivine, but closer to that of olivine at equilibrium. These assessments based on crystal chemical principles are substantiated by *ab initio* calculations (Schauble, 2011). The observations suggest that fractional crystallization of olivine, or partial melting that consumes the pyroxene component in an ultramafic source rock before the olivine, would result in higher $^{26}Mg/^{24}Mg$ in the extracted mafic melts. Experiments are necessary to verify that our expectations based on theory are correct.

A handful of experiments have been done to establish high-temperature Mg isotope partitioning among the mantle minerals. Among them is the study by Macris et al. (2013) in which the three-isotope method was used to investigate Mg isotopic fractionation between pure spinel ($MgAl_2O_4$) and forsterite (Mg_2SiO_4) with magnesite ($MgCO_3$) as the exchange medium. The experimental results yielded the equilibrium Mg isotopic fractionation between spinel and forsterite (expressed as $\delta^{26}Mg_{Spl} - \delta^{26}Mg_{Fo} = \Delta^{26}Mg_{Spl\text{-}Fo} \sim 10^3 ln\alpha_{Spl\text{-}Fo}$) as a function of temperature and are consistent with the predictions based on *ab initio* modeling of bonding in these minerals (Schauble, 2011). The results confirmed that the Mg isotope fractionation between spinel and forsterite observed by Young et al. (2009) in a San Carlos mantle xenolith are consistent with equilibrium isotopic fractionation.

However, these experimental results also show that the Mg isotopic fractionations exhibited by spinel and olivine from mantle xenoliths from the North China Craton (Liu et al., 2011) are lower than would be predicted for pure spinel and forsterite at the temperatures indicated by two-pyroxene cation thermometry in those rocks, and lower than that found by Young et al. (2009). Liu et al. (2011) attribute the lower spinel-olivine Mg isotope fractionation values relative to those reported by Young et al. (2009) mainly to the effects of octahedral-site cation substitutions in spinel following predictions by Schauble (2011). Previous studies proposed that the substitution of Cr or Fe^{3+} for Al in spinel can increase the mean Mg-O bonding length (Hill et al., 1979; O'Neill and Dollase, 1994). This increase in bond length should reduce bond stiffness and lower the affinity for ^{26}Mg over ^{24}Mg relative to that for $MgAl_2O_4$ spinel, yielding smaller $\Delta^{26}Mg_{Spl\text{-}Fo}$ values. This is indeed what was found by Schauble (2011), although until now there has been no experimental confirmation of this prediction.

In this study we apply the three-isotope exchange method (Matsuhisa et al., 1979; Shahar et al., 2008) to experimentally determine the equilibrium Mg isotope fractionation factors between Cr-substituted spinel ($MgAlCrO_4$) and magnesite, and between magnesiochromite ($MgCr_2O_4$) and magnesite as a function of temperature. Magnesite is used as an efficient exchange partner in the experiments (e.g., Clayton et al., 1989; Chacko et al., 1996; Macris et al., 2013). Combined with the Mg equilibrium isotope fractionation factor between forsterite and magnesite determined by Macris et al. (2013), these results determine the influence of Cr substitution in spinel on spinel-forsterite Mg isotopic fractionation.

2. METHOD

2.1. The three-isotope method

Shahar et al. (2008) modified the three-isotope method of Matsuhisa et al. (1979) for application to isotope exchange experiments between two solid phases. This method has been applied to determine fractionation factors

at high temperatures between solids for Fe, Si, Ni, and Mg isotopic systems (e.g., Shahar et al., 2009, 2011; Lazar et al., 2012; Macris et al., 2013). Textural evidence suggests that annealing and recrystallization are the mechanisms of isotope exchange (Macris et al., 2013). We present a brief introduction of this method here.

Fig. 1 shows the principle of the three-isotope method. We rely on the mass fractionation relationship between three isotopes (numbered 1, 2, and 3, here) using two isotope ratios, 2/1 and 3/1, with the same denominator. Using the usual delta notation to indicate fractional differences in the isotope ratios, $\delta^{2/1}$ and $\delta^{3/1}$, the three-isotope plot is constructed by plotting $\delta^{2/1}$ vs. $\delta^{3/1}$. In the present context, $\delta^{2/1}$ and $\delta^{3/1}$ correspond to δ^{25}Mg and δ^{26}Mg, respectively. Incomplete isotope exchange between two phases can be used to acquire the equilibrium fractionation factor by extrapolating the results to the three-isotope condition for isotopic equilibrium. In the case of Mg isotope ratios, this necessary condition for equilibrium is

$$\delta^{25}\mathrm{Mg} = \left(10^3 + \delta^{25}\mathrm{Mg}_{\mathrm{bulk}}\right)\left(\frac{10^3 + \delta^{26}\mathrm{Mg}}{10^3 + \delta^{26}\mathrm{Mg}_{\mathrm{bulk}}}\right)^{\beta} - 10^3 \quad (1)$$

where the exponent β is equal to 0.521 at equilibrium and is based on the expression for Mg equilibrium mass fractionation (Young et al., 2002),

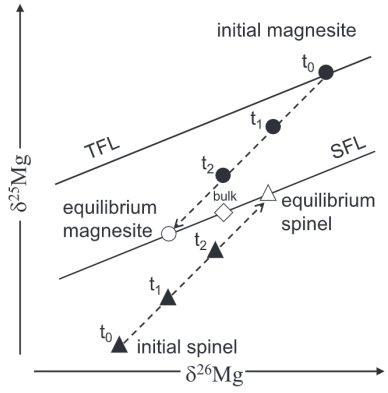

Fig. 1. Schematic diagram of the three-isotope exchange method showing the terrestrial fractionation line (TFL) which reflects the fractionation of natural samples, and the secondary fractionation line (SFL) with the same slope (β) as the TFL but with a different intercept due to the presence of ^{24}Mg-spiked spinel in the system. Varying lengths of exchange time (t_i) result in commensurate degrees of isotope exchange between magnesite and spinel. The data for both phases define lines that can be extrapolated to the SFL to obtain the equilibrium compositions. The bulk composition remains constant throughout the experiment.

$$\beta = \frac{\left(\frac{1}{m_{24}} - \frac{1}{m_{25}}\right)}{\left(\frac{1}{m_{24}} - \frac{1}{m_{26}}\right)} \quad (2)$$

where m_i is the precise mass of isotope i. Equilibrium isotopic compositions in a system with a specified bulk isotopic composition will plot on the secondary fractionation line (SFL) that includes the bulk composition (Fig. 1). The slightly concave fractionation relationship obtained from Eq. (1) can be treated approximately as a straight line with a slope of β and an intercept determined by the bulk isotopic composition of the experimental exchange system. The three-isotope method takes advantage of this condition for equilibrium by using starting materials that lie far from the SFL. This is accomplished by spiking one of the starting phases with the denominator isotope, in this case ^{24}Mg. Experiments run at different durations produce a time series in which the degree of exchange varies. With exchange, the isotope ratios of the reactants move towards the SFL with time. The trajectories towards equilibrium are usually linear within the precision of the measurements, permitting extrapolation to the equilibrium compositions that lie on the SFL. The validity of linear extrapolation is further validated by the observation that analyses are usually mixtures of starting material which has remained unreacted during the experiment and re-equilibrated material, making the lines defined by the data tantamount to mixing lines in three-isotope space between the initial and equilibrated compositions (Shahar and Young, 2020).

The veracity of equilibrium isotope fractionation factors obtained using the three-isotope method have been questioned recently due to potential kinetic effects (Cao and Bao, 2017; Bourdon et al., 2018). To address these concerns, Shahar and Young (2020) showed that the impact from kinetic isotopic effects is insignificant relative to analytical uncertainties using fayalite-magnetite Fe isotopic fractionation as an example. In the present study, Mg is one of the major elements in both starting phases, minimizing these potential effects. We explore the potential for kinetic effects in Section 4.1 and in the Supplemental Online Material.

2.2. Mg isotope exchange experiments

Reactant magnesiochromite, $MgCr_2O_4$, and $MgCrAlO_4$ were synthesized using reagent-grade (>99% pure) magnesite ($MgCO_3$), Al_2O_3 and Cr_2O_3 and two different MgO preparations spiked with ^{24}Mg. The MgO and Al_2O_3 were fired in a muffle furnace at 800 ℃ for several hours prior to mixing. An equimolar mixture of the isotopically spiked MgO and Cr_2O_3 was made and ground in a mortar and pestle dry for 30 minutes. This mixture was pelletized using a steel die and 10-ton press. The mix was extracted from the die as a large pellet along with a few loose pieces of debris. All recovered material was placed in a Pt crucible and fired at 1400 ℃ for 120 hrs to synthesize $MgCr_2O_4$. This process was repeated but with a 2:1:1 molar mixture of ^{24}Mg-spiked MgO, Cr_2O_3, and Al_2O_3 to synthesize $MgCrAlO_4$. Later, when more batches of $MgCr_2O_4$ and $MgCrAlO_4$ were needed for experiments, a second set of

fusions was conducted for 66 hrs. For the 120-hr mix, 0.4 grams of $MgCrAlO_4$ and 0.35 g $MgCr_2O_4$ were produced. For the 66-hr mix, 0.15 grams of $MgCrAlO_4$ and 0.15 g of $MgCr_2O_4$ were produced. On average, measured aliquots are considered accurate to better than ±0.004 g. For the Mg isotope exchange experiments, a 1:1 molar mixture of $MgCr_2O_4$ and $MgCO_3$ and a 1:1 molar mixture of $MgCrAlO_4$ and $MgCO_3$ were used with the ^{24}Mg excesses in the $MgCr_2O_4$ and $MgCrAlO_4$ phases.

To verify that this synthesis technique yielded the desired phases, spiked samples of $MgCr_2O_4$ synthesized for 48 hrs and 120 hrs, and $MgCrAlO_4$ produced by fusion for 120 hrs were generated using the procedure described above and analyzed by X-ray diffraction (XRD) at the University of Rochester. The XRD patterns for the $MgCr_2O_4$ samples indicate that both the 48-hr and 120-hr fusion products have identical peaks that are consistent with magnesiochromite (Fig. 2). The $MgCrAlO_4$ diffraction pattern shows peaks shifted relative to $MgCr_2O_4$ as expected.

The full piston cylinder assembly and their lengths from top to bottom consisted of an MgO piece (~15.2 mm) capable of allowing a thermocouple wire above the experiment, a small MgO plate (~1.0 mm) beneath this, a fired pyrophyllite cup (~12.7 mm) holding the Ag capsule and lid, and finally a MgO plug (~13.6 mm) at the bottom. These components were placed in a graphite furnace that was surrounded by NaCl pressure media. Experimental mixes were contained within the Ag capsules. The "stock" material consisted of an Ag cylinder 7.3 mm in diameter and 9 mm in length. Two separate sample wells were drilled, each with a diameter of 2.1 mm and depth of approximately 6.8 mm, allowing each piston cylinder experiment to do the dual work of both a $MgCr_2O_4$:$MgCO_3$ and $MgCrAlO_4$:$MgCO_3$ Mg isotope exchange experiment. A mixture of Co-CoO was placed at the bottom of each sample well to buffer oxygen fugacity (f_{O2}) to about 0.6 log units below the quartz-fayalite-magnetite (QFM) equilibrium during the experiment. To prevent direct contact and interaction of the experimental charge with the Co-CoO buffer material, thin Ag plates were cut and placed with tweezers above the buffer mix before the experimental mixes were added in each sample well. Experimental mixes (either $MgCr_2O_4$:$MgCO_3$ or $MgCrAlO_4$:$MgCO_3$) were added and packed down with a metal rod in each well until no more material could be placed in the sample well. Experiments varied in the exact amount of material that could be loaded due to slightly different conditions such as the amounts of buffer added to the sample well, along with some variability in well depth for some of the experiments, but it was common for a sample well to be loaded with ~25 mg of experimental reactant. An Ag lid (1.2 mm in height) with the same diameter as the capsule was placed above the capsule. Before heating, each experiment sat at the target 1 GPa pressure for at least 7 hours, providing time for the Ag lid and capsule to pressure seal. All experiments used a heating ramp rate of 100 ℃/min. Temperature was monitored during the experiment using a Type C (25%WRe-3%WRe) thermocouple.

Experiments were conducted at three temperatures of 600, 700, and 800 ℃ of varied duration. Experiments conducted at 700 and 800 ℃ used the $MgCr_2O_4$ and $MgCrAlO_4$ that had been synthesized for 120 hrs. The experiments at 600 ℃ used the $MgCr_2O_4$ and $MgCrAlO_4$ synthesized for 66 hrs. The uncertainties of temperatures in our isotopic exchange experiments are around ±2 °C. The run products were then carefully extracted from the Ag capsules without any buffer material for further separation and isotopic analyses.

2.3. Sample separation and chemical purification

Experimental products were weighed and transferred into Savillex vials for phase separation. The protocol of magnesite-spinel separation was described previously by Macris et al. (2013). To fully dissolve magnesite without

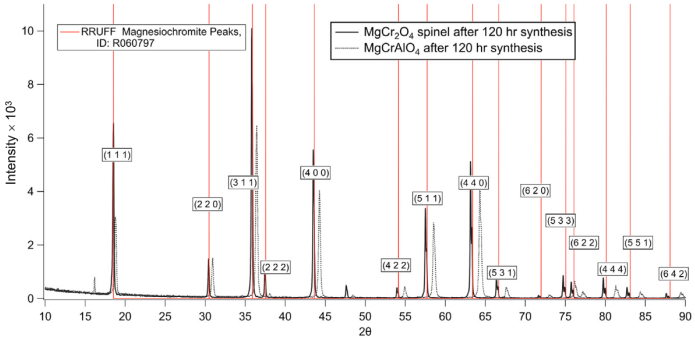

Fig. 2. X-ray diffraction patterns of synthetic Cr-bearing spinel ($MgAlCrO_4$; dash black line) and magnesiochromite ($MgCr_2O_4$; solid black line) compared with RRUFF reference magnesiochromite pattern (red line; e.g., O'Neill and Dollase, 1994; Nestola et al., 2014; Bosi et al., 2019). (For interpretation of the references to color in this figure legend, the reader is referred to the web version of this article.)

leaching spinel, 1 ml of warm 1 N HCl (~120 °C) was added in the vials containing the product mixtures. The vials were sonicated for 5–10 min, and then centrifuged for ~2 min to separate solid spinel from the solution. The liquid containing dissolved magnesite was collected into separate 15 mL Savillex beakers through filter paper to preclude any unwanted suspended solids remaining in the liquid. This procedure was repeated three times with warm HCl and then twice more with ~100 °C Millipore H_2O. The collected liquid containing dissolved magnesite was than dried at 125 °C and redissolved in 1 mL 0.5 N HCl for chemical purification. The solid spinel grains were transferred to 3 mL Savillex beakers for acid digestion.

Spinel grains were digested in a 1:1 mixture of concentrated Omnitrace HF (~29 N) and HNO_3 (~14 N) at temperature of ~220 °C for 72 hrs in Parr bombs. The dissolved samples were evaporated to dryness at 125 °C, redissolved in aqua regia ($HCl:HNO_3 = 2:1$), and placed on a hot plate at 120 °C for 24 hrs. The sample solutions were then dried down and redissolved in 0.5 N HCl in preparation for Mg purification.

Magnesium from spinel and magnesite was purified using ion exchange chromatography in HEPA filtered laminar flow boxes in a class 100 clean laboratory. The purification procedure was modified from Young et al. (2009) and Wombacher et al. (2009) and is described in greater detail in the Supplementary Online Material. We used BioRad 10 mL columns filled with 2 mL of AG50W-X8 resin in 200–400 mesh hydrogen form. Before loading the samples, the resin was washed with Milli-Q water and triply distilled hydrochloride acid with the sequence of 10 mL Milli-Q water, 10 mL 0.5 N HCl, 15 mL 6 N HCl, 10 mL Milli-Q water, and 15 mL 6 N HCl, followed by conditioning with 10 mL 0.5 N HCl. Approximately 0.5 to 1 mL sample volumes in 0.5 N HCl were loaded on the columns. The samples comprised ~30–50 μg of Mg. Chromium and alkali elements (Na and K) were eluted with 34 mL 0.5 N HCl. Aluminum was removed with 7 mL of 0.15 N HF. The columns were then washed with 2 mL Milli-Q water followed by addition of 9 mL of 95% acetone-0.5 N HCl to remove Fe. The remaining acetone in the resin was eliminated by passing 3 mL Milli-Q water through the columns. Removal of acetone is critical because HCl-acetone mixtures can self-catalyze to increase the viscosity of the purified solution and produce matrix effects during isotopic analysis. After washing away acetone, Mg was eluted from the resin by loading 12 mL 2 N HCl. The entire column chemistry procedure was repeated 3 to 5 times, depending on Cr concentration in the sample solutions, to guarantee that the Cr:Mg ratios in the Mg sample solutions were less than 1:100. After Mg purification, the Mg sample solutions were dried down and then redissolved in 2% HNO_3 for isotopic analysis. The yields of Mg after the entire purification procedure of all the samples are >99%. The Mg blank is ~20 ng, negligible relative to the amount of Mg processed through the column procedure. In addition, two well-characterized geostandards, BHVO-2 and DTS-02, were digested, chemically purified, and analyzed simultaneously with the exchanged samples to monitor the accuracy of the analytical procedures.

The efficacy of the separation protocol was tested by applying it to mixtures of our reactant magnesite and spinel that were not subjected to exchange experiments and comparing the results with those for the pure starting materials (i.e., pure aliquots of reactant spinel and magnesite). We followed the same procedures used for the piston cylinder experimental run products for these tests. Magnesium isotopic compositions of the various digested samples were analyzed by MC-ICPMS (Section 2.4). If the separation protocol is efficient, we expect to see no differences in the results for the mixtures and the pure phases. Indeed, we find no differences in isotopic compositions between the pure minerals and those extracted using our separation methods (Table 1), indicating that our method does not lead to cross-contamination between spinel and magnesite.

2.4. Mass spectrometry

Magnesium isotopic measurements were performed on a Thermo-Finnigan Neptune MC-ICPMS in the Department of Earth, Planetary, and Space Sciences at UCLA. The instrument has an array of 9 Faraday collectors. Prior to Mg isotopic analyses, mass scans were performed on each sample to assess the levels of ^{23}Na, ^{27}Al, ^{44}Ca, ^{52}Cr, and ^{56}Fe relative to the Mg concentration to avoid any potential effects of isobaric interferences or matrix effects on Mg isotope ratio measurements. In all cases the abundances of these elements were below 1% of the analyte Mg concentration (see Supplementary Online Material). We analyzed the samples using wet plasma with a quartz dual cyclonic spray chamber. The uptake flow rate was 50 μL/min. Faraday cups L3, L2, C, H1, and H2 with amplifier resistors of 10^{11} Ω were used to measure ^{23}Na, ^{24}Mg, ^{25}Mg, ^{26}Mg, and ^{27}Al, respectively. Data for each sample were collected in 9 blocks with each block consisting of 20 cycles with an integration time of 8 s per cycle. The instrumental fractionation was corrected by sample-standard bracketing, with standard and sample being run in alternate blocks. Cross contamination between samples and standards was eliminated by rinsing the spray chamber with 2% HNO_3 for 3 minutes after each block. The ^{24}Mg signal in the rinse is ~8 mV. Sample and standard solutions were diluted to ~2 ppm Mg in 2% HNO_3 for isotopic analyses. The ^{24}Mg sensitivity was typically ~10 V/ppm (1×10^{-10} amps/ppm). The isotopic signals were measured on flat-top ion beam peaks at a resolution of $M/\Delta M \sim 6000$. Uncertainties for each datum are reported as 2 standard errors (2se). We used DSM3 as the primary Mg isotopic standard (Galy et al., 2003).

2.5. Analytical errors and their propagation

The experimental isotopic fractionation factors ($\Delta^{26}Mg_{Spl\text{-}Mgs}$) between spinel and magnesite in our study are obtained from the intersections between linear regression lines of the time series experiments and the SFL in three-isotope space. The uncertainties in the retrieved $\Delta^{26}Mg_{Spl\text{-}Mgs}$ values are propagated from the regression errors arising from the measurement uncertainties. The method of uncertainty propagation was given by Shahar

Table 1
Mg isotopic compositions of geostandards, starting materials, and experimental samples corresponding to different experimental conditions.

Experiment condition	Sample	Time (min)	Mineral	δ^{25}Mg	2se	δ^{26}Mg	2se
Terrestrial geostandards	BHVO-2			−0.125	0.008	−0.226	0.011
	DTS-02			−0.142	0.019	−0.254	0.030
Magnesite-spinel [$Mg(AlCr)O_4$] in 800 ℃	Starting_Mag_Al_Cr_sp_800*	0	Magnesite	−1.417	0.022	−2.744	0.013
	Mag_Al_Cr_sp_800_0[m]	0	Magnesite	−1.403	0.030	−2.738	0.025
	Mag_Al_Cr_sp_800_15	15	Magnesite	−1.901	0.014	−3.188	0.021
	Mag_Al_Cr_sp_800_60	60	Magnesite	−1.992	0.018	−3.276	0.039
	Mag_Al_Cr_sp_800_120	120	Magnesite	−2.075	0.023	−3.359	0.043
	Mag_Al_Cr_sp_800_240	240	Magnesite	−2.171	0.013	−3.444	0.015
	Starting_Al_Cr_sp_800**	0	Spinel [$Mg(AlCr)O_4$]	−8.804	0.012	−9.460	0.024
	Al_Cr_sp_800_0[m]	0	Spinel [$Mg(AlCr)O_4$]	−8.809	0.020	−9.521	0.032
	Al_Cr_sp_800_15	15	Spinel [$Mg(AlCr)O_4$]	−8.079	0.012	−8.745	0.017
	Al_Cr_sp_800_60	60	Spinel [$Mg(AlCr)O_4$]	−8.121	0.034	−8.776	0.068
	Al_Cr_sp_800_120	120	Spinel [$Mg(AlCr)O_4$]	−8.070	0.013	−8.746	0.023
	Al_Cr_sp_800_240	240	Spinel [$Mg(AlCr)O_4$]	−7.925	0.009	−8.582	0.022
Magnesite-magnesiochromite in 800 ℃	Starting_Mag_Cr_sp_800*	0	Magnesite	−1.417	0.022	−2.744	0.013
	Mag_Cr_sp_800_0[m]	0	Magnesite	−1.395	0.012	−2.707	0.024
	Mag_Cr_sp_800_15	15	Magnesite	−3.297	0.010	−4.520	0.009
	Mag_Cr_sp_800_60	60	Magnesite	−3.473	0.015	−4.706	0.015
	Mag_Cr_sp_800_120	120	Magnesite	−3.588	0.011	−4.797	0.014
	Mag_Cr_sp_800_240	240	Magnesite	−3.792	0.015	−4.992	0.019
	Starting_Cr_sp_800***	0	Magnesiochromite	−9.806	0.013	−10.546	0.009
	Cr_sp_800_0[m]	0	Magnesiochromite	−9.816	0.010	−10.486	0.018
	Cr_sp_800_15	15	Magnesiochromite	−8.527	0.009	−9.288	0.010
	Cr_sp_800_60	60	Magnesiochromite	−8.346	0.013	−9.150	0.014
	Cr_sp_800_120	120	Magnesiochromite	−8.242	0.011	−8.991	0.011
	Cr_sp_800_240	240	Magnesiochromite	−7.505	0.010	−8.328	0.010
Magnesite-spinel [$Mg(AlCr)O_4$] in 700 ℃	Starting_Mag_Al_Cr_sp_700*	0	Magnesite	−1.417	0.022	−2.744	0.013
	Mag_Al_Cr_sp_700_15	15	Magnesite	−1.681	0.014	−2.996	0.021
	Mag_Al_Cr_sp_700_60	60	Magnesite	−1.754	0.016	−3.064	0.030
	Mag_Al_Cr_sp_700_120	120	Magnesite	−1.865	0.018	−3.179	0.016
	Mag_Al_Cr_sp_700_240	240	Magnesite	−1.937	0.022	−3.239	0.039
	Mag_Al_Cr_sp_700_480	480	Magnesite	−1.985	0.008	−3.280	0.017
	Starting_Al_Cr_sp_700**	0	Spinel [$Mg(AlCr)O_4$]	−8.804	0.012	−9.460	0.024
	Al_Cr_sp_700_15	15	Spinel [$Mg(AlCr)O_4$]	−8.651	0.046	−9.349	0.085
	Al_Cr_sp_700_60	60	Spinel [$Mg(AlCr)O_4$]	−8.530	0.010	−9.205	0.017
	Al_Cr_sp_700_120	120	Spinel [$Mg(AlCr)O_4$]	−8.471	0.007	−9.178	0.013
	Al_Cr_sp_700_240	240	Spinel [$Mg(AlCr)O_4$]	−8.405	0.010	−9.074	0.024
	Al_Cr_sp_700_480	480	Spinel [$Mg(AlCr)O_4$]	−8.303	0.011	−8.961	0.017
Magnesite-magnesiochromite in 700 ℃	Starting_Mag_Cr_sp_700*	0	Magnesite	−1.417	0.022	−2.744	0.013
	Mag_Cr_sp_700_15	15	Magnesite	−2.228	0.010	−3.542	0.013
	Mag_Cr_sp_700_60	60	Magnesite	−2.545	0.014	−3.855	0.018
	Mag_Cr_sp_700_120	120	Magnesite	−2.641	0.009	−3.939	0.010
	Mag_Cr_sp_700_240	240	Magnesite	−2.816	0.008	−4.105	0.011
	Mag_Cr_sp_700_480	480	Magnesite	−2.827	0.020	−4.124	0.025
	Starting_Cr_sp_700***	0	Magnesiochromite	−9.806	0.013	−10.546	0.009

(*continued on next page*)

Table 1 (*continued*)

Experiment condition	Sample	Time (min)	Mineral	δ^{25}Mg	2se	δ^{26}Mg	2se
	Cr_sp_700_15	15	Magnesiochromite	−9.686	0.009	−10.420	0.011
	Cr_sp_700_60	60	Magnesiochromite	−9.522	0.010	−10.290	0.007
	Cr_sp_700_120	120	Magnesiochromite	−9.411	0.009	−10.146	0.010
	Cr_sp_700_240	240	Magnesiochromite	−9.408	0.012	−10.209	0.012
	Cr_sp_700_480	480	Magnesiochromite	−9.049	0.008	−9.825	0.010
Magnesite-spinel [$Mg(AlCr)O_4$] in 600 ℃	Starting_Mag_Al_Cr_sp_600*	0	Magnesite	−1.417	0.022	−2.744	0.013
	Mag_Al_Cr_sp_600_60	60	Magnesite	−1.831	0.018	−3.139	0.014
	Mag_Al_Cr_sp_600_120	120	Magnesite	−1.962	0.014	−3.265	0.010
	Mag_Al_Cr_sp_600_240	240	Magnesite	−1.964	0.019	−3.280	0.014
	Mag_Al_Cr_sp_600_3d	4320	Magnesite	−2.071	0.010	−3.368	0.021
	Starting_Al_Cr_sp_600	0	Spinel [$Mg(AlCr)O_4$]	−9.277	0.015	−9.902	0.011
	Al_Cr_sp_600_60	60	Spinel [$Mg(AlCr)O_4$]	−8.601	0.008	−9.215	0.010
	Al_Cr_sp_600_120	120	Spinel [$Mg(AlCr)O_4$]	−8.308	0.011	−8.919	0.012
	Al_Cr_sp_600_240	240	Spinel [$Mg(AlCr)O_4$]	−8.053	0.012	−8.674	0.023
	Al_Cr_sp_600_3d	4320	Spinel [$Mg(AlCr)O_4$]	−7.937	0.014	−8.514	0.010
Magnesite-magnesiochromite in 600 ℃	Starting_Mag_Cr_sp_600*	0	Magnesite	−1.417	0.022	−2.744	0.013
	Mag_Cr_sp_600_60	60	Magnesite	−1.643	0.019	−2.917	0.011
	Mag_Cr_sp_600_120	120	Magnesite	−1.679	0.017	−2.942	0.018
	Mag_Cr_sp_600_240	240	Magnesite	−1.731	0.017	−2.942	0.021
	Mag_Cr_sp_600_3d	4320	Magnesite	−2.473	0.012	−3.772	0.013
	Starting_Cr_sp_600	0	Magnesiochromite	−9.233	0.010	−9.846	0.019
	Cr_sp_600_60	60	Magnesiochromite	−8.857	0.014	−9.519	0.021
	Cr_sp_600_120	120	Magnesiochromite	−8.691	0.007	−9.355	0.010
	Cr_sp_600_240	240	Magnesiochromite	−8.336	0.012	−9.018	0.017
	Cr_sp_600_3d	4320	Magnesiochromite	−8.741	0.015	−9.367	0.018

* All magnesite starting material samples share the same source, and therefore the same isotopic value.
[m] The samples are only mixed without experiecing exchange experiment to testify the reliability of separation protocol.
** The starting spinel [$Mg(AlCr)O_4$] samples for the experiments of 700℃ and 800℃ were synthesized together.
*** The starting magnesiochromite samples for the experiments of 700℃ and 800℃ were synthesized together.

et al. (2008) for Fe isotope fractionation factors between magnetite and fayalite. Here we briefly describe the application of this method for Mg isotope fractionation in spinel-magnesite system.

The intersections of δ^{26}Mg values between the regression lines for the minerals and the SFL are calculated using the expression

$$\delta^{26}Mg_{Eq,i} = \frac{-b_1 + b_2}{m_1 - \beta} \tag{3}$$

where $\delta^{26}Mg_{Eq,i}$ represents the equilibrium δ^{26}Mg value obtained by extrapolation of the regression lines to the SFL for mineral i, m_1 and b_1 correspond to the slope and intercept of the regression line for mineral i, and β and b_2 are the slope and intercept of the SFL, respectively (here $\beta_{Mg} = 0.521$). The uncertainty in each isotope ratio measurement is the 2 standard error (2 se) of 9 analyses of the same sample solution. We applied the new "York" regression (Mahon, 1996) to obtain a linear regression of the data points for each temperature. The uncertainties in $\Delta^{26}Mg_{Spl\text{-}Mgs}$ values are estimated based on the intersections of the error envelopes (Ludwig, 1980) for the regressions of the spinel or magnesite data with the SFL. The δ^{26}Mg values for the intersection between the SFL and the error envelopes can be calculated using

$$\delta^{26}_{Error\text{ - }SFL} = \left(\pm\left(\sigma^4_{m_1}\bar{\delta^{26}}^2 + 2\sigma^2_{m_1}\bar{\delta^{26}}(\beta - m_1)(b_2 - b_1) + \beta^2\sigma^2_{b_1} - 2\beta\sigma^2_{b_1}m_1 + b_2^2\sigma^2_{m_1} - 2b_2b_1\sigma^2_{m_1} + b_1^2\sigma^2_{m_1} + \sigma^2_{b_1}\left(m_1^2 - \sigma^2_{m_1}\right)\right)^{1/2} - \sigma^2_{m_1}\bar{\delta^{26}} + (\beta - m_1)(b_1 - b_2)\right) / \beta^2 - 2\beta m_1 - \sigma^2_{m_1} + m_1^2 \tag{4}$$

where $\delta^{26}_{Error\text{ - }SFL}$ is the δ^{26}Mg intersection of the error envelope with the SFL, σ_{b_1} and σ_{m_1} are the uncertainties in the intercept and slope for the regression line, and $\bar{\delta^{26}}$ is the centroid, or weighted mean, of δ^{26}Mg values for the mineral at the given temperature. These standard errors for the equilibrium $\delta^{26}Mg_{Spl}$ and $\delta^{26}Mg_{Mgs}$ values are then propagated to the final $\Delta^{26}Mg_{Spl\text{-}Mgs}$ by adding them in quadrature. The resulting errors in $\Delta^{26}Mg_{Spl\text{-}Mgs}$ values are reported as 2 se at each temperature and the initial mineral combination ($MgAlCrO_4$-$MgCO_3$ or $MgCr_2O_4$-$MgCO_3$).

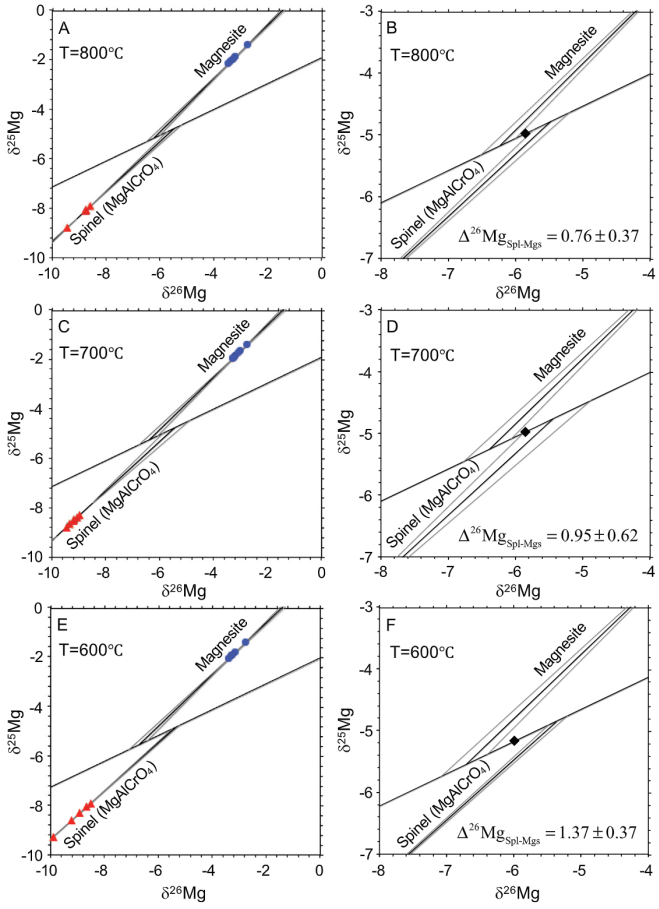

Fig. 3. Experimental results for magnesite (blue dots) and Cr-bearing spinel ($MgAlCrO_4$, red triangles) at 800 °C (A and B), 700 °C (C and D), and 600 °C (E and F). Panels B, D, and F are close-ups of the intersections for the data shown in panels A, C, and E, respectively. The bulk compositions are represented by black diamonds. The regression lines and envelops are calculated using the new "York" regression (Mahon, 1996). Uncertainties are 2se. (For interpretation of the references to color in this figure legend, the reader is referred to the web version of this article.)

Finally, the $\Delta^{26}Mg_{Spl\text{-}Mgs}$ values at each temperature are regressed for the two mineral pairs (Mahon, 1996) to obtain the equation for $\Delta^{26}Mg_{Spl\text{-}Mgs}$ and its uncertainty as a function of temperature. The Python code to calculate $\Delta^{26}Mg_{Spl\text{-}Mgs}$ values and their standard errors is provided in the supporting online material.

3. RESULTS

3.1. Spinel-magnesite experiments

A summary of the Mg isotopic values obtained as part of this study is given in Table 1. The Mg isotopic composi-

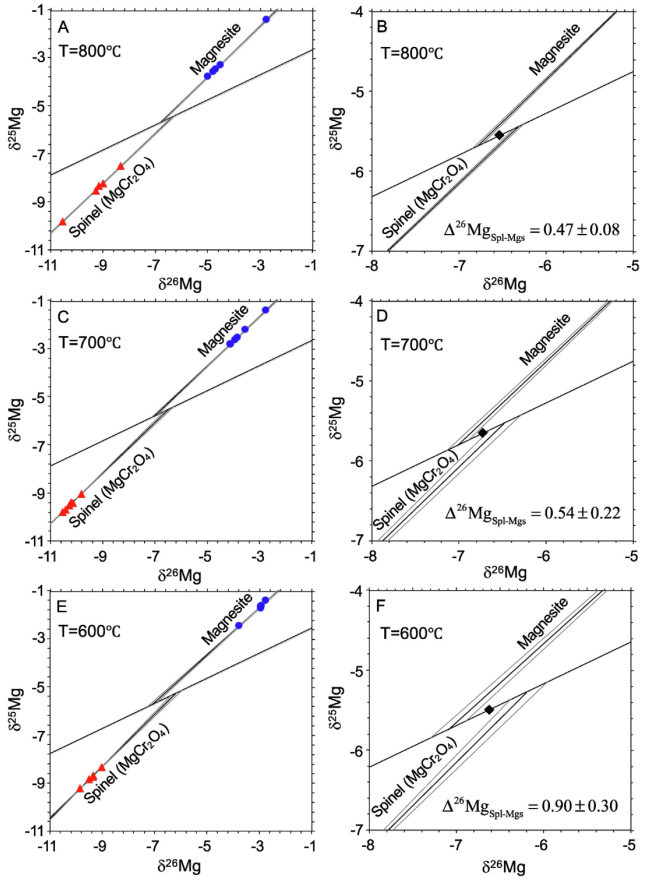

Fig. 4. Experimental results for magnesite (blue dots) and magnesiochromite ($MgCr_2O_4$, red triangles) at 800 °C (A and B), 700 °C (C and D), and 600 °C (E and F). Panels B, D, and F are close-ups showing the intersections defined by the data in panels A, C, and E, respectively. The bulk compositions are represented by black diamonds. The regression lines and envelops are calculated using the new "York" regression (Mahon, 1996). Uncertainties are 2se. (For interpretation of the references to color in this figure legend, the reader is referred to the web version of this article.)

tions obtained from two geostandards, BHVO-2 and DTS-02, are identical to the reference values within uncertainties ($\delta^{26}Mg_{BHVO\text{-}02} = -0.20 \pm 0.07‰$, $\delta^{26}Mg_{DTS\text{-}02} = -0.32 \pm 0.06‰$; Teng et al., 2015). We show the Mg isotope ratios for the products of exchange experiments conducted at 1 GPa at 800 °C, 700 °C, and 600 °C. To achieve resolvable isotopic exchange, the experiments at 800 °C were performed for 15, 60, 120, and 240 mins, the 700 °C experiments for 15, 60, 120, 240, and 480 mins, and the 600 °C experiments for 60, 120, 240, and 4320 mins (72 hrs, or 3 days).

None of the experimental run products have compositions directly on the secondary fractionation lines, indicating that none of these experiments came to complete isotopic equilibrium (Figs. 3 and 4). The equilibrium Mg isotope ratios of spinel and magnesite were therefore obtained by extrapolation to the SFLs. For the experiments involving exchange of Mg between $MgAlCrO_4$ and

$MgCO_3$, extrapolation of the regressed data to intersection with the SFLs yields $\Delta^{26}Mg_{Spl\text{-}Mgs}$ values of $0.76 \pm 0.37‰$ at 800 °C (Fig. 3A and B), $0.95 \pm 0.62‰$ at 700 °C (Fig. 3C and D), and $1.37 \pm 0.37‰$ at 600 °C (Fig. 3E and F). For $MgCr_2O_4$-$MgCO_3$ exchange experiments, extrapolation of the regressed data to the SFLs at each temperature yields $\Delta^{26}Mg_{Spl\text{-}Mgs}$ values of $0.47 \pm 0.08‰$ at 800 °C (Fig. 4A and B), $0.54 \pm 0.22‰$ at 700 °C (Fig. 4C and D), and $0.90 \pm 0.30‰$ at 600 °C (Fig. 4E and F).

3.2. Spinel-forsterite fractionation

In order to use our equilibrium spinel-magnesite fractionation factors to obtain the fractionations between Cr-substituted spinel and forsterite, we combine our results with the forsterite-magnesite exchange experiments of Macris et al. (2013) that were obtained using a similar set of experiments. While similar, details of the implementation of the data reduction method are slightly amended from the study by Macris et al. (2013) (apparently due to the significant figures used in the codes). We therefore recalculated the Macris et al. (2013) fractionation factors from the data for internal consistency. Although well within quoted uncertainties, the recalculated fractionation factors are slightly different from those in the published study. The re-calculated $\Delta^{26}Mg_{Fo\text{-}Mgs}$ values based on the data of Macris et al. (2013) and our slightly modified data reduction code are $0.08 \pm 0.06‰$ at 800 °C (cf. the published value of $0.04 \pm 0.04‰$), $0.11 \pm 0.17‰$ at 700 °C (cf. the published value of $0.11 \pm 0.10‰$), and $0.32 \pm 0.15‰$ at 600 °C (cf. the published value of $0.44 \pm 0.10‰$). The combination of our new measured spinel-magnesite fractionation factors and the forsterite-magnesite values yields equilibrium $\Delta^{26}Mg_{Spl\text{-}Fo}$ values between Cr-substituted spinel ($MgAlCrO_4$) and forsterite of $0.68 \pm 0.37‰$ at 800 °C, $0.85 \pm 0.64‰$ at 700 °C, and $1.04 \pm 0.40‰$ at 600 °C. The equilibrium fractionation factor between magnesiochromite and forsterite yields $\Delta^{26}Mg_{Spl\text{-}Fo}$ values of $0.39 \pm 0.10‰$ at 800 °C, $0.44 \pm 0.27‰$ at 700 °C, and $1.58 \pm 0.33‰$ at 600 °C.

3.3. Temperature-related equilibrium Mg isotope fractionation

The experimentally determined $MgAlCrO_4$-magnesite and $MgCr_2O_4$-magnesite fractionation factors are plotted as a function of exchange temperature in Fig. 5. Linear regression of these data provides equations for spinel-magnesite fractionation factors as a function of temperature:

$$\Delta^{26}Mg_{MgAlCrO_4\text{ - }Mgs} = (0.96 \pm 0.22) \times 10^6/T^2 \quad (5)$$

and

$$\Delta^{26}Mg_{MgCr_2O_4\text{ - }Mgs} = (0.55 \pm 0.08) \times 10^6/T^2. \quad (6)$$

Regression of the data from Macris et al. (2013), with slight modification due to recalculating the regression line-SFL intersections, leads to slightly revised equations for the temperature-dependent forsterite-magnesite and pure spinel-magnesite fractionation factors:

$$\Delta^{26}Mg_{Fo\text{ - }Mgs} = (0.12 \pm 0.06) \times 10^6/T^2 \quad (7)$$

and

$$\Delta^{26}Mg_{MgAl_2O_4\text{ - }Mgs} = (1.17 \pm 0.27) \times 10^6/T^2, \quad (8)$$

where temperature T is in K in all cases. Equations (7) and (8) are consistent with the equations obtained from regression of Macris et al. (2013) within uncertainties. The uncertainties reflect propagation of 2 standard errors through the linear regression. The spinel-forsterite temperature-dependent fractionation factors obtained from Equations (5)–(8) are:

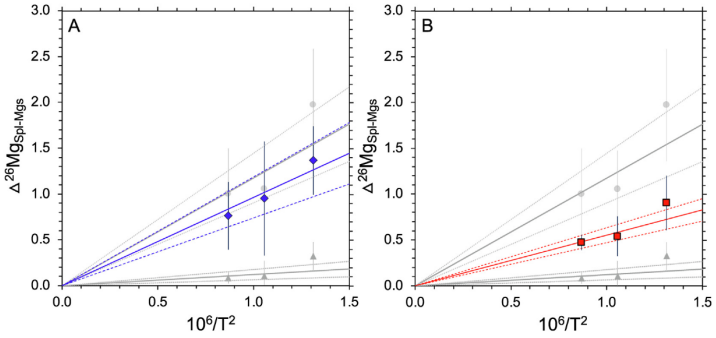

Fig. 5. (A) Experimental Cr-bearing spinel-magnesite (blue diamonds and blue line) and (B) magnesiochromite-magnesite (red rectangles and red line) Mg isotope fractionation as a function of temperature. Also shown are previous data for pure spinel-magnesite (grey dots and upper grey line) and forsterite-magnesite (grey triangles and lower grey line) from the experiments by Macris et al. (2013). Thick lines are linear best-fits through the data and thin dash lines are error envelops derived by propagation of 2se analytical uncertainties. (For interpretation of the references to color in this figure legend, the reader is referred to the web version of this article.)

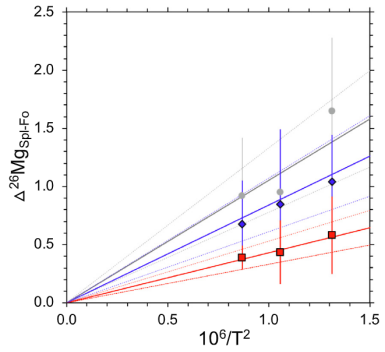

Fig. 6. Experimental spinel-forsterite Mg isotope fractionation with varying Cr substitution for Al in spinel as determined by Macris et al. (2013) and this study, including pure spinel (no Cr substitution, grey dots and grey line), Cr-bearing spinel (50% Cr substitution, blue diamonds and blue line), and magnesiochromite (100% Cr substitution, red rectangles and red line). Thick lines are linear best-fits through the data and thin dash lines are error envelops derived by propagation of 2se analytical uncertainties. (For interpretation of the references to color in this figure legend, the reader is referred to the web version of this article.)

$$\Delta^{26}Mg_{MgAl_2O_4\text{ - Fo}} = (1.05 \pm 0.28) \times 10^6/T^2 \quad (9)$$

$$\Delta^{26}Mg_{MgAlCrO_4\text{ - Fo}} = (0.84 \pm 0.23) \times 10^6/T^2 \quad (10)$$

$$\Delta^{26}Mg_{MgCr_2O_4\text{ - Fo}} = (0.43 \pm 0.10) \times 10^6/T^2. \quad (11)$$

The experimental results and best-fit regression lines for the three temperatures for pure spinel-forsterite, Cr-bearing spinel ($MgAlCrO_4$)-forsterite, and magnesiochromite-forsterite are shown in Fig. 6.

4. DISCUSSION

4.1. Accuracy of three-isotope method for spinel-magnesite exchange experiment

Cao and Bao (2017) argued that the isotope exchange between two reservoirs can be dominated by kinetic effects – instead of α_{eq} – resulting in an unreliable experimental α_{eq} value. They used oxygen isotopes shared between minerals and either liquids or vapor water as the examples. Shahar and Young (2020) applied the kinetic formalism for isotope exchange developed previously by Northrop and Clayton (1966) and Criss et al. (1987), and adopted by Cao and Bao (2017), to investigate the accuracy of the three-isotope method for the exchange experiment between two solid phases where kinetics are involved. Shahar and Young (2020) found that the impact from kinetic isotopic effects, exemplified by differences in isotope diffusion rates in the experiments, would impart departures from true equilibrium values on the order of ~0.01‰ using fayalite-magnetite Fe isotopic fractionation as an example. They also noted that because the trajectories of the time series defined by the data are in part mixing lines between unequilibrated and equilibrated materials, the effects of kinetics are further mitigated.

Bourdon et al. (2018) proposed that for the case where the element of interest is a minor or trace component, changes in mineral chemistry during the experiments would change the target equilibrium isotope ratios in three-isotope space. This would occur because the relative proportions of the element of interest contained in the exchanging phases would change. Shahar and Young (2020) showed with numerical simulations – for typical experimental designs – that this effect is smaller than the analytical precision even when the analyte concentration in the phase changes by many tens of per cent of the initial value. Here we apply the kinetic formalism for isotope exchange of Mg isotopes between magnesiochromite and magnesite following Shahar and Young (2020) to estimate the potential for errors that might arise in the experiments themselves.

Following Shahar and Young (2020), we consider Mg isotope exchange between two phases, x and y by the reaction:

$$^{24}Mg_x + {}^{25}Mg_y \underset{k}{\overset{\alpha_{Eq}{}^{25}k}{\rightleftharpoons}} {}^{25}Mg_x + {}^{24}Mg_y \quad (12)$$

where α_{Eq} is the equilibrium isotope fractionation factor and k is the rate constant for the exchange process with units of s^{-1}. The equilibrium isotopic fractionation factor α_{Eq} is equivalent to the equilibrium constant for the reaction in Equation (12), such that

$$\alpha_{Eq} = K_{Eq} = \frac{[{}^{25}Mg_x]}{[{}^{25}Mg_x]}\frac{[{}^{24}Mg_y]}{[{}^{25}Mg_y]} = \frac{\left({}^{25}Mg/{}^{24}Mg\right)_x}{\left({}^{25}Mg/{}^{24}Mg\right)_y} = \frac{R_{x,Eq}}{R_{y,Eq}}. \quad (13)$$

In closed systems like our experiments, the rates of change of the isotope ratios R_x and R_y for phases x and y are also constrained by the relation

$$X_x\frac{dR_x}{dt} + X_y\frac{dR_y}{dt} = 0, \quad (14)$$

where X_x and X_y are the fractions of total Mg in the experimental charge residing in phases x and y, respectively. Equations (13) and (14) require that the rates of change of R_x and R_y are

$$\frac{dR_x}{dt} = k\left(\alpha_{Eq}R_y - R_x\right) \quad (15)$$

and

$$\frac{dR_y}{dt} = -k\frac{X_x}{X_y}\left(\alpha_{Eq}R_y - R_x\right), \quad (16)$$

respectively. We emphasize that the product $\alpha_{Eq}R_y$ is the isotope ratio that phase x would have if it were in equilibrium with phase y at time t. It is the difference between this ratio and the actual ratio R_x at any given time that drives the exchange reaction. Upon integration, and with substitution of the definition of the equilibrium fractionation factor, one obtains for the isotope ratios for phase x (Shahar and Young, 2020)

$$\ln\left\{\frac{R_{x,\mathrm{Eq}}-R_x(t)}{R_{x,\mathrm{Eq}}-R_x^0}\right\}=-kt\left\{\frac{\alpha_{\mathrm{Eq}}X_x}{X_y}\right\}, \tag{17}$$

where $R_{x,\mathrm{Eq}}$ is the equilibrium isotope ratio for phase x and $R_x(t)$ is the ratio for phase x at time t. Here we consider no changes in X_x and X_y during the experiments due to net transfer reactions that would cause the proportions of the phases and their Mg concentrations to change (see discussion in the Supplemental Online Material). The left-hand side of Equation (17) can be represented by the fractional approach to equilibrium for phases x, f_x ranging from 0 to 1 (e.g., Criss et al., 1987)

$$\frac{R_{x,\mathrm{Eq}}-R_x(t)}{R_{x,\mathrm{Eq}}-R_x^0}=1-\frac{R_x(t)-R_x^0}{R_{x,\mathrm{Eq}}-R_x^0}=1-f_x. \tag{18}$$

Substitution into Equation (17) yields

$$f_x=\frac{\delta_x(t)-\delta_x^0}{\delta_{x,\mathrm{Eq}}-\delta_x^0}=1-\exp\left(-kt\frac{\alpha_{\mathrm{Eq}}X_x}{X_y}\right). \tag{19}$$

The equation for the fractional approach to equilibrium as a function of time provides the means to examine possible discrepancies between the true (or ideal) and observed isotopic fractionation factors obtained using the three-isotope method (Shahar and Young, 2020). Fig. 7A shows in schematic form potential inaccuracies in the derived fractionation factors based on differences in equilibration rates between the two Mg isotope ratios. The prospects for inaccuracies are cast in terms of the ideal slope in three-isotope space defined by the initial and true equilibrium isotope ratios:

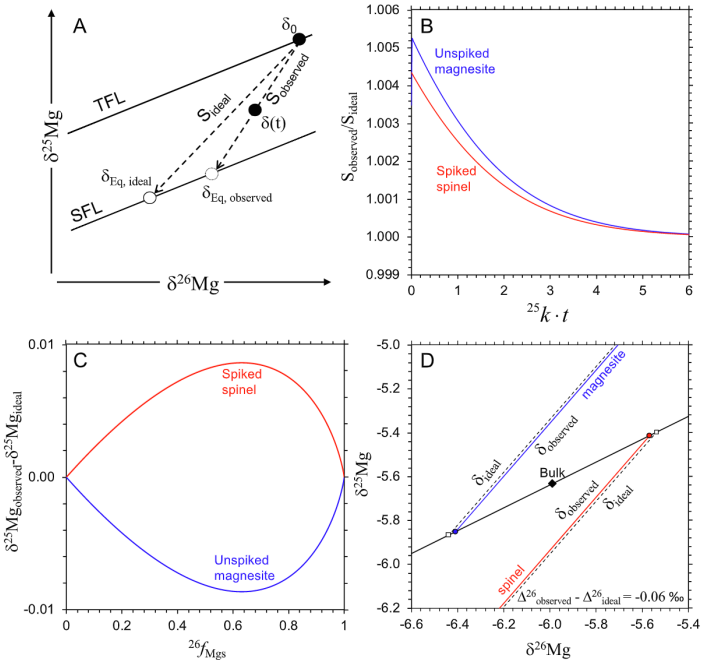

Fig. 7. Plots comparing ideal exchange in Mg three-isotope space with exchange limited by unequal rates of diffusion of ^{25}Mg and ^{26}Mg isotopes. (A) Schematic Mg three-isotope plot showing the relationships between the observed and ideal/true three-isotope slopes for a single phase during an exchange experiment (see text). (B) The ratio of observed slope to ideal slope as a function of e-folding time for isotopic exchange. The differences between the observed and ideal slopes diminishes with time. (C) Calculated differences in the observed and ideal δ^{25}Mg values for magnesite and spinel where rates of exchange are limited by diffusion as a function of the extent of equilibration, $^{26}f_{\mathrm{Mgs}}$. (D) Results of a numerical simulation of a three-isotope exchange experiment in the spinel-magnesite Mg system analogous to our actual experiment at 600 °C. The ideal $\Delta^{26}\mathrm{Mg}_{\mathrm{Spl\text{-}Mgs}}$ is 0.9‰ and $^{25}k \cdot t$ is ~ 0.27. The calculated difference between the ideal (white rectangles) compositions with equal rate constants and compositions where unequal diffusivities are rate limiting (blue and red dots for magnesite and spinel, respectively) generates a shift of ~ 0.06‰ for $\Delta^{26}\mathrm{Mg}_{\mathrm{Spl\text{-}Mgs}}$ compared to the ideal value. (For interpretation of the references to color in this figure legend, the reader is referred to the web version of this article.)

$$S_{\text{ideal}} = \frac{\delta_x^{25}\text{Mg}_{\text{Eq}} - \delta_x^{25}\text{Mg}^0}{\delta_x^{26}\text{Mg}_{\text{Eq}} - \delta_x^{26}\text{Mg}^0} \tag{20}$$

and the observed slope:

$$S_{\text{observed}} = \frac{\delta_x^{25}\text{Mg}(t) - \delta_x^{25}\text{Mg}^0}{\delta_x^{26}\text{Mg}(t) - \delta_x^{26}\text{Mg}^0} \tag{21}$$

where $\delta_x^i\text{Mg}(t)$ is the time-dependent isotope ratio for phase x expressed in delta notation, $\delta_x^i\text{Mg}_{\text{Eq}}$ is the isotope ratio for phase x prescribed by equilibrium between phases x and y, and $\delta_x^i\text{Mg}^0$ is the initial isotopic composition at time zero for phase x. Following the general approach described by Cao and Bao (2017), Shahar and Young (2020) showed that Equations (18)–(21) can be used to derive the ratio of the observed slope in three-isotope space to the true, or ideal, slope defined by the difference between the initial and equilibrium isotope ratios:

$$\frac{S_{\text{observed}}}{S_{\text{ideal}}} = \frac{f_x^{25}}{f_x^{26}} = \frac{1 - \exp\left(-\,{}^{25}kt\frac{\alpha_{\text{Eq}}^{25} X_x}{X_y}\right)}{1 - \exp\left(-\,{}^{26}kt\frac{\alpha_{\text{Eq}}^{26} X_x}{X_y}\right)}. \tag{22}$$

Equation (22) shows that any disparity between observed and true three-isotope slopes will arise when the rate constants for $^{25}\text{Mg}/^{24}\text{Mg}$ and $^{26}\text{Mg}/^{24}\text{Mg}$ exchange, ${}^{25}k$ and ${}^{26}k$, are different. We regard the likelihood for differences in these rate constants due to mineral dissolution and reprecipitation (Ostwald ripening) that evidently occurs in our experiments to be vanishingly low. Therefore, the maximum differences would be the result of the mass-dependent diffusion of Mg isotopes in the two solid phases during the experiments. In this case, ${}^{25}k/\,{}^{26}k = {}^{25}D/\,{}^{26}D$. The ratio of diffusivities can be estimated using

$$\frac{{}^{25}D}{{}^{26}D} = \left(\frac{m_{26}}{m_{25}}\right)^{\lambda_{\text{Mg}}}, \tag{23}$$

where the exponent λ_{Mg} can be constrained based on diffusion experiments. Sio et al. (2018) suggested $\lambda_{\text{Mg}} = 0.09 \pm 0.05$ for forsteritic olivine. Due to the absence of experiments for λ_{Mg} for spinel and magnesite, here we use $\lambda_{\text{Mg}} \sim 0.1$ to derive a value for $^{25}\text{k}/^{26}\text{k} \sim {}^{25}\text{D}/^{26}\text{D} = 1.00392$. The resulting ratio of rate constants applied to Equation (22) produces the time-dependent values for $S_{\text{observed}}/S_{\text{ideal}}$ shown in Fig. 7B. The $S_{\text{observed}}/S_{\text{ideal}}$ ratio starts from the maximum value of 1.00525 at the beginning of the experiment and declines to unity as exchange proceeds. Note that to construct Fig. 7B we treat the unspiked, isotopically normal magnesite as phase x and calculate $S_{\text{observed}}/S_{\text{ideal}}$ for magnesite with $\alpha_{\text{mgs-spl}}$. We then assign phase x as the ^{24}Mg-spiked spinel and use $\alpha_{\text{spl-mgs}}$ to calculate $S_{\text{observed}}/S_{\text{ideal}}$ for the spiked spinel. The abscissa is in units of e-folding time (${}^{25}k \cdot t$) for the reaction. After ~5 e-folding times for exchange (${}^{25}k \cdot t = 5$), the observed slopes for both reactant phases are indistinguishable from their respective ideal slopes ($S_{\text{observed}}/S_{\text{ideal}} \sim 1$), implying that the experiments approach equilibrium with no discernible inaccuracies due to the different rates of ^{25}Mg and ^{26}Mg self-diffusion. The Mg isotopic composition of phase x associated with exchange duration t as a function of departures from the ideal slope can be obtained from

$$\delta_x^{25}\text{Mg}(t)_{\text{observed}} = \delta_x^{25}\text{Mg}^0 + \left(\delta_x^{26}\text{Mg}(t) - \delta_x^{26}\text{Mg}^0\right) S_{\text{ideal}} \frac{{}^{25}f_x}{{}^{26}f_x}. \tag{24}$$

Since ${}^{25}f_x/{}^{26}f_x = 1$ for the ideal case, any discrepancy between the observed and ideal $\delta_x^{25}\text{Mg}$ values at time t is

$$\delta_x^{25}\text{Mg}(t)_{\text{observed}} - \delta_x^{25}\text{Mg}(t)_{\text{ideal}} = \left(\delta_x^{26}\text{Mg}(t) - \delta_x^{26}\text{Mg}^0\right) S_{\text{ideal}} \left(\frac{{}^{25}f_x}{{}^{26}f_x} - 1\right). \tag{25}$$

Fig. 7C shows the calculated variations in $\delta_{\text{mgs}}^{25}\text{Mg}_{\text{observed}} - \delta_{\text{mgs}}^{25}\text{Mg}_{\text{ideal}}$ and $\delta_{\text{spl}}^{25}\text{Mg}_{\text{observed}} - \delta_{\text{spl}}^{25}\text{Mg}_{\text{ideal}}$ as functions of ${}^{26}f_{\text{mgs}}$ if the disparities in isotope diffusion were rate limiting in the experiments. The Mg isotopic compositions for the spiked spinel (phase y in this calculation) are calculated from mass balance. The largest departures from the ideal δ^{25}Mg values are on the order of 0.01‰, which occurs at ~60% exchange.

Assuming that isotope diffusion was rate limiting, we use Equation (25) to examine the potential impact of unequal rate constants for exchange on our final derived fractionation factors. We find that the impact of different rates of diffusion is negligible. As an illustration, we use the data for the exchange between magnesiochromite and magnesite at 600 °C. In these experiments, $X_{\text{mgs}} = X_{\text{spl}} = 0.5$. Assuming for this exercise that the derived $\Delta^{26}\text{Mg}_{\text{spl-mgs}}$ of 0.9‰ is the correct, or ideal, value, we calculate that for a shift in the reactant phases of ~1‰, comparable to the shifts in the magnesiochromite-magnesite experiment at 600 °C, the discrepancy in δ^{25}Mg at the given δ^{26}Mg value imposed by unequal rate constants for exchange is ~0.0048‰, resulting in a shift in the δ^{26}Mg intersection with the SFL of ~0.03‰. The derived value for $\Delta^{26}\text{Mg}_{\text{Spl-Mgs}}$ is then 0.84‰, differing from the assumed correct value by 0.06‰. This potential aberration is small in comparison to the uncertainty of ±0.30‰ for the fractionation factor at this temperature.

4.2. Comparison to theoretical calculations

In this section we compare our experimentally determined equilibrium fractionation factors with predictions from theory. Schauble (2011) used density functional perturbation theory (DFPT) to calculate vibrational frequencies for a number of Mg-bearing crystalline structures, including those investigated here. The results were used to derive reduced partition function ratios and mineral-mineral $^{26}\text{Mg}/^{24}\text{Mg}$ fractionation factors over a range of temperatures. The temperature-dependent forsterite-magnesite, spinel-magnesite, and magnesiochromite-magnesite fractionation factors from Schauble (2011), expressed in per mil, are

$$\Delta^{26}\text{Mg}_{\text{Fo - Mgs}} = 0.34 \times 10^6/T^2 \tag{26}$$

$$\Delta^{26}\text{Mg}_{\text{MgAl}_2\text{O}_4\text{-Mgs}} = 1.32 \times 10^6/T^2 \tag{27}$$

$$\Delta^{26}Mg_{MgCr_2O_4\text{ - }Mgs} = 0.67 \times 10^6/T^2. \quad (28)$$

There is no direct calculation for $\Delta^{26}Mg_{MgAlCrO_4\text{ - }Mgs}$. These results predict a lower $^{26}Mg/^{24}Mg$ ratio in magnesite relative to those in coexisting spinel and forsterite due to the relatively longer mean Mg—O bond in the carbonate that reduces the Mg—O bond stiffness. This first-order observation is verified by the experiments (Fig. 8A). The spinel-magnesite fractionation factors, both for pure spinel and magnesiochromite, are similar to the DFPT predictions in view of the uncertainties in the experimental results (Fig. 8). However, the DFPT values for $\Delta^{26}Mg_{Fo\text{ - }Mgs}$ are significantly greater than the experimental values determined by Macris et al. (2013), as previously noted by those authors. This discrepancy between experimental results and theoretical calculations is even greater when compared with some other recent *ab initio* calculations (Wu et al., 2015; Wang et al., 2017). In all cases, the calculations agree with the experiments in that forsterite concentrates the heavy Mg isotopes relative to magnesite. The lower value for $\Delta^{26}Mg_{Fo\text{ - }Mgs}$ obtained from the experiments is closer to the fractionation predicted by the purely ionic model for bonding using the Mg—O bond lengths in magnesite (Young et al., 2015). Regardless, the source of the discrepancy between theory and experiments in this case is not known but could be due to inaccuracies in the calculations, inaccuracies in the experiments, or a combination of both.

The DFPT estimates for $\Delta^{26}Mg_{Spl\text{ - }Fo}$ for pure spinel and magnesiochromite as functions of temperature are

$$\Delta^{26}Mg_{MgAl_2O_4\text{ - }Fo} = 0.98 \times 10^6/T^2 \quad (29)$$

and

$$\Delta^{26}Mg_{MgCr_2O_4\text{ - }Fo} = 0.34 \times 10^6/T^2. \quad (30)$$

These predictions are within experimental uncertainties of the values derived from our experiments (Fig. 8B). This good agreement between theory and experiments for the spinel-forsterite fractionation factors suggests that the discrepancy between theory and experiments for the forsterite-magnesite fractionation cancel; taken as a whole, four of the five fractionation factors evaluated here show good agreement between theory and experiments.

4.3. Impact from Cr substitution on spinel-olivine Mg isotope geothermonetry

Previous studies have reported small but resolvable inter-mineral $^{26}Mg/^{24}Mg$ isotope fractionation between coexisting pyroxene, olivine, spinel, and other minerals in mantle rocks (e.g., Handler et al., 2009; Yang et al., 2009; Young et al., 2009; Liu et al., 2011; Xiao et al., 2013; Xiao et al., 2016; Hu et al., 2016; Stracke et al., 2018; Hu et al., 2020). Some of these studies investigated Mg isotope fractionation between coexisting mantle spinel and olivine (Young et al., 2009; Liu et al., 2011; Xiao et al., 2013; Xiao et al., 2016; Stracke et al., 2018). In all mantle xenoliths studied, spinel exhibits higher $^{26}Mg/^{24}Mg$ ratios when compared to coexisting olivine. The degree to which these observed fractionations represent equilibrium in each case warrants closer examination.

Fig. 9A shows spinel-olivine Mg isotope fractionations plotted against temperatures determined independently (Young et al., 2009; Liu et al., 2011; Xiao et al., 2013; Stracke et al., 2018). The temperature-dependent fractionations for pure spinel-forsterite and magnesiochromite-forsterite from theory and from the experiments are shown for comparison. The measured spinel-forsterite fractionation data from Young et al. (2009) fall on the theoretically

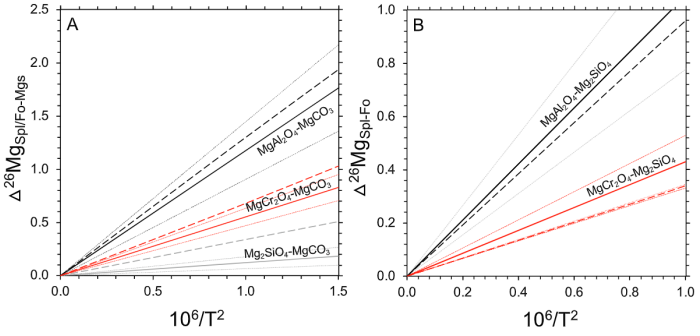

Fig. 8. (A) Experimental results (solid lines) and theoretical predictions (thick dash lines) of equilibrium Mg isotope fractionation of pure spinel-magnesite (black lines), magnesiochromite-magnesite (red lines), and forsterite-magnesite (grey lines) as functions of temperatures. (B) Experimental results (solid lines) and theoretical predictions (thick dash lines) of equilibrium Mg isotope fractionation of pure spinel-forsterite (black lines) and magnesiochromite-forsterite (red lines) yielded from (A). The error envelops, thin dashed lines, are propagated from 2se analytical uncertainties. (For interpretation of the references to color in this figure legend, the reader is referred to the web version of this article.)

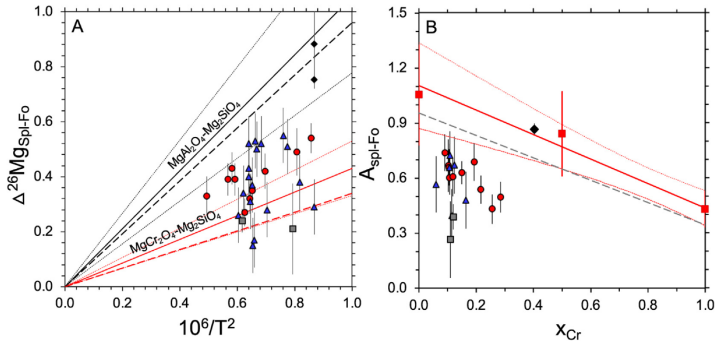

Fig. 9. (A) Comparison of spinel-olivine Mg isotopic fractionations from natural peridotites and xenoliths, including San Carlos xenoliths (black diamonds, Young et al., 2009), north China craton peridotites (red dots, Liu et al., 2011; blue triangles, Xiao et al., 2013), and Hawaiian xenoliths (grey rectangles, Stracke et al., 2018), with experimental and theoretical Mg isotopic fractionation factors between spinel and forsterite. The temperatures for San Carlos xenoliths were estimated based on inversion parameter for Al-Mg ordering in spinel, whereas the temperatures of all other samples were calculated using Cpx-Opx cation thermometry. (B) Correlation between the coefficient $A_{Spl\text{-}Fo}$ in the function $\Delta^{26}Mg_{Spl-Fo} = A_{Spl-Fo} \times 10^6/T^2$ and the mole fraction of Cr in spinel x [x = molar Cr/(Cr + Al)]. The experimental regression line (red solid line) is based on the spinel-forsterite fractionation factors determined by Macris et al. (2013) and in our experiments (red rectangles). The theoretical regression line is represented by the grey dash line based on the calculation in Schauble (2011). Error envelopes are propagated from 2 se analytical errors (thin red dash lines). The data obtained from natural samples are also shown for comparison (symbols are the same as those in panel A). The coefficient $A_{Spl\text{-}Fo}$ for each sample is calculated based on the $\Delta^{26}Mg_{Spl-Ol}$ value and the estimated temperature. Chromium site-specific mole fractions, x_{Cr}, are calculated from the spinel chemical compositions published in the corresponding references. (For interpretation of the references to color in this figure legend, the reader is referred to the web version of this article.)

and experimentally determined pure spinel-forsterite fractionation lines within uncertainties, whereas the data from Liu et al. (2011), Xiao et al. (2013) and Stracke et al. (2018) fall below the pure spinel-forsterite fractionation line, with some data plotting on the magnesiochromite-forsterite fractionation lines within errors (Fig. 9A). Part of the difference between these studies could be the use of different geothermometers to obtain independent estimates of temperature. The temperatures for the samples from the North China craton (NCC) reported by Liu et al. (2011) and Xiao et al. (2013), and those from the Hawaiian Islands reported by Stracke et al. (2018), are all calculated by using the two-pyroxene cation thermometer (Brey and Köhler, 1990; Wells, 1977). Previous studies have revealed a wide range of cation-based temperatures (528–1236 °C) for the peridotites from NCC (Wu et al., 2006). On the other hand, Young et al. (2009) compared the Mg isotopic fractionation factor with the inversion parameter for Mg-Al ordering in spinels from the Group I xenoliths from San Carlos (Uchida et al., 2005). In these rocks, the spinel inversion parameter temperature of 808 °C ± 37 is consistent with the Mg isotope temperature of 814 °C ± 60 obtained from the spinel and forsterite Mg isotope fractionation and the DFPT temperature calibration from Schauble (2011).

Another variable to consider when evaluating the likelihood that Mg isotope fractionation between spinel and forsterite represents an equilibration temperature is the cation substitution for Al in the spinels. Most xenolith spinel grains in the studies discussed above have varying degrees of substitution for Al. As predicted by theory (Schauble, 2011) and verified here by experiments, the proclivity of spinel to concentrate ^{26}Mg (and ^{25}Mg) over ^{24}Mg depends on the substitution of other cations for Al. The general structural formula for spinel is $^{IV}(R^{2+}_{1-i}, R^{3+}_{i})^{VI}(R^{2+}_{i}, R^{3+}_{2-i})O_4$ where R^{2+} and R^{3+} represent divalent and trivalent cations, respectively. In typical mantle spinels, i is close to zero, and Al^{3+} fills the octahedral coordinated cation site; the spinels are "normal". In this case Mg is indeed mainly tetrahedrally coordinated. Substitution of Cr or Fe^{3+} for Al in the octahedral site can increase the mean Mg—O bond length (Schauble, 2011) and reduce the affinity of the tetrahedral site for the heavy Mg isotopes.

Because the mantle spinels are neither end-member spinel nor end-member magnesiochromite, we require a continuous relationship between Cr substitution for Al and spinel-forsterite Mg isotope fractionation. We measured the fractionation for three different degrees of $CrAl_{-1}$ substitution, so the resulting three calibrations, Equations (9), (10), and (11), allow us to derive a relationship for the temperature-dependent fractionation of $^{26}Mg/^{24}Mg$ between spinel and forsterite as a function of Cr replacement for Al in these normal spinels. Fig. 9B shows the correlation between the mole fraction of Cr in spinel, x, where x = Cr/(Cr + Al) on a molar basis, and the coefficient $A_{Spl\text{-}Fo}$ in the expression $\Delta^{26}Mg_{Spl\text{-}Fo} = A_{Spl\text{-}Fo} \times 10^6/T^2$. From linear regression of this relationship one obtains the desired function for $\Delta^{26}Mg_{spinel\text{-}forsterite}$ as a function of temperature and Cr mole fraction:

$$\Delta^{26}Mg_{Mg(Al_{1-x}Cr_x)_2O_4\ -\ Fo} = [(-0.67 \pm 0.26)x + 1.10 \pm 0.23] \times \frac{10^6}{T^2}, \quad (31)$$

The validity of the linear relationship in Equation (31) is supported by the agreement, within uncertainties, between the linear fit to the experiments and the two-point line obtained from the *ab initio* DFPT calculations by Schauble (2011) for pure spinel and magnesiochromite (Fig. 9B).

Equation (31) can be used to further assess the likelihood that the spinel-olivine fractionations measured in the mantle xenoliths represent equilibrium. We do this by estimating values for $A_{Spl\text{-}Fo}$ for each natural sample based on the measured values for $\Delta^{26}Mg_{Spl\ -\ Fo}$, the independent estimates for the temperatures of equilibration, and the Cr fraction x as reported for the spinels. Note that we exclude the data from spinels with relatively significant Fe content (Mg#<75) to avoid the unknown isotopic effects of Fe substitution on octahedral and tetrahedral sites. Most data lie outside of the error envelope associated with Equation (31) (Fig. 9B). Only the sample from the San Carlos xenolith is consistent with Equation (31), implying that the combination of the observed Mg isotope fractionation between spinel and olivine, the Cr content of the spinels, and the spinel inversion parameter equilibration temperature of ~800 °C are consistent with isotopic equilibrium at this temperature. The deviation of the other data from the experimental calibration may be the result of differences in the closure temperatures of inter-mineral Mg isotopic equilibration and inter-mineral cation equilibration as suggested by Stracke et al. (2018). Temperatures for the xenoliths from NCC and Hawaii were estimated based on two-pyroxene Ca and Fe-Mg exchange between clino- and orthopyroxene (Brey and Köhler, 1990). Wu et al. (2006) proposed a large range of equilibrium temperatures for NCC xenoliths (528–1236 °C) using various geothermometers, imparting considerable uncertainties for reconciling the cation thermometry and the Mg isotope fractionations. In addition, Mg isotopic disequilibrium is known to occur in mantle rocks. Mg isotope fractionations between clinopyroxene and olivine from San Carlos xenolith suggested an equilibrium temperature of 300–400 °C, much lower than that estimated from spinel-olivine Mg isotope fractionation (~800 °C) (Young et al., 2009). Three possible explanations for this temperature discordance were proposed, including incorrect theoretical predictions, analytical artifacts during Mg isotope measurement of the pyroxenes, and disequilibrium of Mg isotopes between olivine (Ol), clinopyroxene (Cpx), and orthopyroxene (Opx) as a result of metasomatism or exchange with a partial melt. Among these explanations the last possibility was highlighted given the greater mobility of the Cpx component in the mantle relative to Ol and spinel (e.g., Gudfinnsson and Presnall, 2000) and extensive Li isotope disequilibrium in pyroxenes in a San Carlos spinel lherzolite (e.g., Jeffcoate et al., 2007).

5. CONCLUSIONS

We applied the three-isotope exchange method to experimentally determine the equilibrium Mg isotope fractionation factors between Cr-bearing spinel and magnesite as functions of temperature. Resolvable Mg isotope exchange was obtained between the two mineral phases at 600, 700, and 800 °C. Combining these results with earlier determinations of the equilibrium fractionation between forsterite and magnesite allow us to determine the equilibrium isotope fractionation factors between Cr-bearing spinel and forsterite. The experimental fractionation factors for magnesiochromite ($MgCr_2O_4$)-magnesite and magnesiochromite-forsterite are in agreement with theoretical predictions within uncertainties. Changes in spinel-forsterite Mg isotope fractionation vary approximately linearly with the substitution of Cr for Al in spinel. This correlation allows us to formulate an experimentally-calibrated Mg isotope fractionation factor between spinel and forsterite as a function of both temperature and Cr substitution for Al in spinel. When applied to natural samples, the combination of measured Mg isotope fractionation between spinel and forsterite, the Cr concentrations of the spinels, and estimates of temperature from independent geothermometers can be used to identify differences in closure temperatures between Mg isotope exchange and cation exchange, and/or disequilibrium. Further studies are required to explore the effects of substitutions of other cations, such as Fe, on Mg isotope fractionation factors involving normal spinels.

Declaration of Competing Interest

The authors declare that they have no known competing financial interests or personal relationships that could have appeared to influence the work reported in this paper.

ACKNOWLEDGEMENT

We acknowledge Stefan Weyer, Shichun Huang, Merlin Méheut, and an anonymous reviewer for their constructive reviews. We thank Adam Ianno for his contribution to the development of the chromatography procedure for Mg purification. This work was supported by NSF EAR-1524811 to EDY and NSF EAR-1751903 to DT.

APPENDIX A. SUPPLEMENTARY MATERIAL

Supplementary data to this article can be found online at https://doi.org/10.1016/j.gca.2020.12.028.

REFERENCES

Bourdon B., Tipper E. T., Fitoussi C. and Stracke A. (2010) Chondritic Mg isotope composition of the Earth. *Geochim. Cosmochim. Acta* **74**, 5069–5083.

Bourdon B., Roskosz M. and Hin R. C. (2018) Isotope tracers of core formation. *Earth Sci. Rev.* **181**, 61–81.

Bosi F., Biagioni C. and Pasero M. (2019) Nomenclature and classification of the spinel supergroup. *Eur. J. Mineral.* **31**, 183–192.

Brey G. P. and Köhler T. (1990) Geothermobarometry in four-phase lherzolites II. New thermobarometers, and practical assessment of existing thermobarometers. *J. Petrol.* **31**, 1353–1378.

Cao X. and Bao H. (2017) Redefining the utility of the three-isotope method. *Geochim. Cosmochim. Acta* **212**, 16–32.

Chacko T., Hu X., Mayeda T. K., Clayton R. N. and Goldsmith J. R. (1996) Oxygen isotope fractionations in muscovite, phlogopite, and rutile. *Geochim. Cosmochim. Acta* **60**, 2595–2608.

Clayton R. N., Goldsmith J. R. and Mayeda T. K. (1989) Oxygen isotope fractionation in quartz, albite, anorthite and calcite. *Geochim. Cosmochim. Acta* **53**, 725–733.

Criss R. E., Gregory R. T. and Taylor, Jr, H. P. (1987) Kinetic theory of oxygen isotopic exchange between minerals and water. *Geochim. Cosmochim. Acta* **51**, 1099–1108.

Dauphas N., Teng F. Z. and Arndt N. T. (2010) Magnesium and iron isotopes in 2.7 Ga Alexo komatiites: mantle signatures, no evidence for Soret diffusion, and identification of diffusive transport in zoned olivine. *Geochim. Cosmochim. Acta* **74**, 3274–3291.

Galy A., Yoffe O., Janney P. E., Williams R. W., Cloquet C., Alard O., Halicz L., Wadhwa M., Hutcheon I. D., Ramon E. and Carignan J. (2003) Magnesium isotope heterogeneity of the isotopic standard SRM980 and new reference materials for magnesium-isotope-ratio measurements. *J. Anal. At. Spectrom.* **18**, 1352–1356.

Gudfinnsson G. H. and Presnall D. C. (2000) Melting behaviour of model lherzolite in the system CaO–MgO–Al_2O_3–SiO_2–FeO at 0.7–2.8 GPa. *J. Petrol.* **41**, 1241–1269.

Jeffcoate A. B., Elliott T., Kasemann S. A., Ionov D., Cooper K. and Brooker R. (2007) Li isotope fractionation in peridotites and mafic melts. *Geochim. Cosmochim. Acta* **71**, 202–218.

Handler M. R., Baker J. A., Schiller M., Bennett V. C. and Yaxley G. M. (2009) Magnesium stable isotope composition of Earth's upper mantle. *Earth Planet. Sci. Lett.* **282**, 306–313.

Hill R. J., Craig J. R. and Gibbs G. V. (1979) Systematics of the spinel structure type. *Phys. Chem. Miner.* **4**, 317–339.

Hin R. C., Coath C. D., Carter P. J., Nimmo F., Lai Y. J., von Strandmann P. A. P., Willbold M., Leinhardt Z. M., Walter M. J. and Elliott T. (2017) Magnesium isotope evidence that accretional vapour loss shapes planetary compositions. *Nature* **549**, 511–515.

Hu Y., Teng F. Z., Zhang H. F., Xiao Y. and Su B. X. (2016) Metasomatism-induced mantle magnesium isotopic heterogeneity: evidence from pyroxenites. *Geochim. Cosmochim. Acta* **185**, 88–111.

Hu Y., Teng F.-Z. and Ionov D. A. (2020) Magnesium isotopic composition of metasomatized upper sub-arc mantle and its implications to Mg cycling in subduction zones. *Geochim. Cosmochim. Acta* **278**, 219–234.

Huang F., Zhang Z., Lundstrom C. C. and Zhi X. (2011) Iron and magnesium isotopic compositions of peridotite xenoliths from Eastern China. *Geochim. Cosmochim. Acta* **75**, 3318–3334.

Lazar C., Young E. D. and Manning C. E. (2012) Experimental determination of equilibrium nickel isotope fractionation between metal and silicate from 500 °C to 950 °C. *Geochim. Cosmochim. Acta* **86**, 276–295.

Li W. Y., Teng F. Z., Xiao Y. and Huang J. (2011) High-temperature inter-mineral magnesium isotope fractionation in eclogite from the Dabie orogen, China. *Earth Planet. Sci. Lett.* **304**, 224–230.

Liu S. A., Teng F. Z., Yang W. and Wu F. Y. (2011) High-temperature inter-mineral magnesium isotope fractionation in mantle xenoliths from the North China craton. *Earth Planet. Sci. Lett.* **308**, 131–140.

Ludwig K. R. (1980) Calculation of uncertainties of U-Pb isotope data. *Earth Planet. Sci. Lett.* **46**, 212–220.

Macris C. A., Young E. D. and Manning C. E. (2013) Experimental determination of equilibrium magnesium isotope fractionation between spinel, forsterite, and magnesite from 600 to 800 °C. *Geochim. Cosmochim. Acta* **118**, 18–32.

Mahon K. I. (1996) The New "York" regression: Application of an improved statistical method to geochemistry. *Int. Geol. Rev.* **38**, 293–303.

Matsuhisa Y., Goldsmith J. R. and Clayton R. N. (1979) Oxygen isotopic fractionation in the system quartz-albite-anorthite-water. *Geochim. Cosmochim. Acta* **43**, 1131–1140.

Nestola F., Periotto B., Andreozzi G. B., Bruschini E. and Bosi F. (2014) Pressure-volume equation of state for chromite and magnesiochromite: A single-crystal X-ray diffraction investigation. *Am. Mineral.* **99**, 1248–1253.

Northrop D. A. and Clayton R. N. (1966) Oxygen-isotope fractionations in systems containing dolomite. *J. Geol.* **74**, 174–196.

O'Neill H. S. C. and Dollase W. A. (1994) Crystal structures and cation distributions in simple spinels from powder XRD structural refinements: $MgCr_2O_4$, Zn Cr_2O_4, Fe_3O_4 and the temperature dependence of the cation distribution in $ZnAl_2O_4$. *Phys. Chem. Miner.* **20**, 541–555.

von Strandmann P. A. P., Elliott T., Marschall H. R., Coath C., Lai Y. J., Jeffcoate A. B. and Ionov D. A. (2011) Variations of Li and Mg isotope ratios in bulk chondrites and mantle xenoliths. *Geochim. Cosmochim. Acta* **75**, 5247–5268.

Schauble E. A. (2011) First-principles estimates of equilibrium magnesium isotope fractionation in silicate, oxide, carbonate and hexaaquamagnesium (2+) crystals. *Geochim. Cosmochim. Acta* **75**, 844–869.

Shahar A., Young E. D. and Manning C. E. (2008) Equilibrium high-temperature Fe isotope fractionation between fayalite and magnetite: an experimental calibration. *Earth Planet. Sci. Lett.* **268**, 330–338.

Shahar A., Ziegler K., Young E. D., Ricolleau A., Schauble E. A. and Fei Y. (2009) Experimentally determined Si isotope fractionation between silicate and Fe metal and implications for Earth's core formation. *Earth Planet. Sci. Lett.* **288**, 228–234.

Shahar A., Hillgren V. J., Young E. D., Fei Y., Macris C. A. and Deng L. (2011) High-temperature Si isotope fractionation between iron metal and silicate. *Geochim. Cosmochim. Acta* **75**, 7688–7697.

Shahar A. and Young E. D. (2020) An assessment of iron isotope fractionation during core formation. *Chem. Geol.* **119800**.

Shannon R. D. (1976) Revised effective ionic radii and systematic studies of interatomic distances in halides and chalcogenides. *Acta Crystallogr. Section A: Crystal Phys. Diffract. Theoret. Gen. Crystallogr.* **32**, 751–767.

Sio C. K., Roskosz M., Dauphas N., Bennett N. R., Mock T. and Shahar A. (2018) The isotope effect for Mg-Fe interdiffusion in olivine and its dependence on crystal orientation, composition and temperature. *Geochim. Cosmochim. Acta* **239**, 463–480.

Stracke A., Tipper E. T., Klemme S. and Bizimis M. (2018) Mg isotope systematics during magmatic processes: Inter-mineral fractionation in mafic to ultramafic Hawaiian xenoliths. *Geochim. Cosmochim. Acta* **226**, 192–205.

Teng F. Z., Wadhwa M. and Helz R. T. (2007) Investigation of magnesium isotope fractionation during basalt differentiation: implications for a chondritic composition of the terrestrial mantle. *Earth Planet. Sci. Lett.* **261**, 84–92.

Teng F. Z., Li W. Y., Ke S., Marty B., Dauphas N., Huang S., Wu F. Y. and Pourmand A. (2010) Magnesium isotopic composition of the Earth and chondrites. *Geochim. Cosmochim. Acta* **74**, 4150–4166.

Teng F. Z., Li W. Y., Ke S., Yang W., Liu S. A., Sedaghatpour F., Wang S. J., Huang K. J., Hu Y., Ling M. X. and Xiao Y. (2015)

Magnesium isotopic compositions of international geological reference materials. *Geostand. Geoanal. Res.* **39**, 329–339.

Uchida H., Lavina B., Downs R. T. and Chesley J. (2005) Single-crystal X-ray diffraction of spinels from the San Carlos Volcanic Field, Arizona: Spinel as a geothermometer. *Am. Mineral.* **90**, 1900–1908.

Wang S. J., Teng F. Z., Williams H. M. and Li S. G. (2012) Magnesium isotopic variations in cratonic eclogites: Origins and implications. *Earth Planet. Sci. Lett.* **359**, 219–226.

Wang W., Qin T., Zhou C., Huang S., Wu Z. and Huang F. (2017) Concentration effect on equilibrium fractionation of Mg-Ca isotopes in carbonate minerals: Insights from first-principles calculations. *Geochim. Cosmochim. Acta* **208**, 185–197.

Wang S. J., Teng F. Z., Li S. G. and Hong J. A. (2014) Magnesium isotopic systematics of mafic rocks during continental subduction. *Geochim. Cosmochim. Acta* **143**, 34–48.

Wells P. R. (1977) Pyroxene thermometry in simple and complex systems. *Contrib. Miner. Petrol.* **62**, 129–139.

Wiechert U. and Halliday A. N. (2007) Non-chondritic magnesium and the origins of the inner terrestrial planets. *Earth Planet. Sci. Lett.* **256**, 360–371.

Wombacher F., Eisenhauer A., Heuser A. and Weyer S. (2009) Separation of Mg, Ca and Fe from geological reference materials for stable isotope ratio analyses by MC-ICP-MS and double-spike TIMS. *J. Anal. At. Spectrom.* **24**, 627–636.

Wu F. Y., Walker R. J., Yang Y. H., Yuan H. L. and Yang J. H. (2006) The chemical-temporal evolution of lithospheric mantle underlying the North China Craton. *Geochim. Cosmochim. Acta* **70**, 5013–5034.

Wu Z., Huang F. and Huang S. (2015) Isotope fractionation induced by phase transformation: first-principles investigation for Mg_2SiO_4. *Earth Planet. Sci. Lett.* **409**, 339–347.

Xiao Y., Teng F. Z., Zhang H. F. and Yang W. (2013) Large magnesium isotope fractionation in peridotite xenoliths from eastern North China craton: product of melt–rock interaction. *Geochim. Cosmochim. Acta* **115**, 241–261.

Xiao Y., Teng F.-Z., Su B.-X., Hu Y., Zhou M.-F., Zhu B., Shi R.-D., Huang Q.-S., Gong X.-H. and He Y.-S. (2016) Iron and magnesium isotopic constraints on the origin of chemical heterogeneity in podiform chromitite from the Luobusa ophiolite, Tibet: Iron and magnesium isotopic constraints. *Geochem. Geophys. Geosyst.* **17**, 940–953.

Yang W., Teng F. Z. and Zhang H. F. (2009) Chondritic magnesium isotopic composition of the terrestrial mantle: a case study of peridotite xenoliths from the North China craton. *Earth Planet. Sci. Lett.* **288**, 475–482.

Young E. D. and Galy A. (2004) The isotope geochemistry and cosmochemistry of magnesium. *Rev. Mineral. Geochem.* **55**, 197–230.

Young E. D., Galy A. and Nagahara H. (2002) Kinetic and equilibrium mass-dependent isotope fractionation laws in nature and their geochemical and cosmochemical significance. *Geochim. Cosmochim. Acta* **66**, 1095–1104.

Young E. D., Tonui E., Manning C. E., Schauble E. and Macris C. A. (2009) Spinel–olivine magnesium isotope thermometry in the mantle and implications for the Mg isotopic composition of Earth. *Earth Planet. Sci. Lett.* **288**, 524–533.

Young E. D., Manning C. E., Schauble E. A., Shahar A., Macris C. A., Lazar C. and Jordan M. (2015) High-temperature equilibrium isotope fractionation of non-traditional stable isotopes: Experiments, theory, and applications. *Chem. Geol.* **395**, 176–195.

Young E. D., Shahar A., Nimmo F., Schlichting H. E., Schauble E. A., Tang H. and Labidi J. (2019) Near-equilibrium isotope fractionation during planetesimal evaporation. *Icarus* **323**, 1–15.

Associate editor: Stefan Weyer